Multi-exposure microscopic image fusion-based detail enhancement algorithm

Harbinder Singh [a], Gabriel Cristobal [b], Gloria Bueno [c,*], Saul Blanco [d], Simrandeep Singh [e], P.N. Hrisheekesha [a], Nitin Mittal [e]

[a] *Chandigarh Engineering College, Landran, Mohali, India*
[b] *Instituto de Optica (CSIC), Serrano 121, Madrid, Spain*
[c] *VISILAB, Univ. Castilla la Mancha, Cuidad Real, Spain*
[d] *Department of Biodiversity and Environmental Management, Universidad de Leon, Leon, Spain*
[e] *Department of Electronics and Communication Engineering, Chandigarh University, Gharuan, Punjab, India*

ARTICLE INFO

ABSTRACT

Traditional microscope imaging techniques are unable to retrieve the complete dynamic range of a diatom species with complex silica-based cell walls and multi-scale patterns. In order to extract details from the diatom, multi-exposure images are captured at variable exposure settings using microscopy techniques. A recent innovation shows that image fusion overcomes the limitations of standard digital cameras to capture details from high dynamic range scene or specimen photographed using microscopy imaging techniques. In this paper, we present a cell-region sensitive exposure fusion (CS-EF) approach to produce well-exposed fused images that can be presented directly on conventional display devices. The ambition is to preserve details in poorly and brightly illuminated regions of 3-D transparent diatom shells. The aforesaid objective is achieved by taking into account local information measures, which select well-exposed regions across input exposures. In addition, a modified histogram equalization is introduced to improve uniformity of input multi-exposure image prior to fusion. Quantitative and qualitative assessment of proposed fusion results reveal better performance than several state-of-the-art algorithms that substantiate the method's validity.

1. Introduction

Diatoms are recognized as vital in the functioning of the ecosystem for the various ecological services they offer, such as CO2 sequestration, O2 production and silica cycling [1]. Freshwater covers only 0.78 percent of the Earth's surface, while marine ecosystems span three-quarters of it. Diatoms are crucial micro-organisms that have distinct biological characteristics to ensure the health of any aquatic ecosystem. They can be sensitive ecosystem change sentinels because of their brief life cycles, which allow them to adapt quickly to their environment. Apart from these features, the fossils on the glass cell walls are marketed as diatomite and have direct commercial worth in various fields such as nutraceuticals, pharmaceuticals and renewal biofuels. Diatom research continues to attract the interest of both basic and applied researchers due to its wide range of applications.

Diatoms may be considered as a fascinating natural work of art, but their study involves careful examination of several delicate microstructures that are scarcely noticeable using low magnification techniques. Diatom sensitivity to environmental parameters means that

they can be used for the detection of changes in water quality, as well as to obtain information on ecological status, on an infinitely more subtle scale than would be obtained using conventional water chemistry techniques. Other application areas of diatom research are forensic science and oil exploration. All of these applications necessitate counting and identifying the various species present in the sample of interest. Complete data is therefore obtained from the specimen before automated identification [2]. Our objective in this paper is to describe a framework for multi-exposure image fusion based detail preservation. Modern optical microscopes can automatically capture and analyze specimen images in order to produce the best possible sample image. Diatoms are microscopic algae, and are classified based on shell contour patterns and pores, called striae. Because diatoms appear in such a broad variety of forms and structures, bright field and dark field microscopy can capture more than one picture with vital and valuable information. A sequence of photographs at variable exposure

---

levels are taken to capture more details. In this case, the concept of image fusion comes into play.

Nonlinear mapping is used by a digital camera with electronic picture array which determines how scene radiance is converted into pixel value in the image captured by the digital microscope. In the early days of photography, photo-sensitive film was used to capture luminance variations present in the scene. In 1947, the experimental setup for the creation of the latent picture was performed primarily in the Kodak Research Laboratories at Rochester and Harrow. An overview of the reactions of the photochemistry of silver halide is presented in [3]. Image processing methods are applied on microscopy images to visualize fine features in the specimen. A post-processing step towards enhancing local contrast was carried out in [4]. Such work highlighted the use of simple averaging filter on atomic force microscopy (AFM). Various topographical features were visible in the processed image. In another approach, low rank denoising was proposed to enhance atomic resolution imaging which improved the signal to noise ratios in the processed images [5]. In general, the proposed image fusion method is utilized to boost local contrast while reducing noise in the fused image. It helps to retain important features present in the specimen under observation.

High Dynamic Range (HDR) image encoding comes into play when full range of color and luminance values need to be captured. HDR laser scanning microscope produces a single image that is correctly exposed in both dark and light areas [6]. For real world imaging, Debevec and Malik [7] used a quadratic objective function based on least square error to recover smooth and monotonic response. In order to exclude pixel values that are saturated, a weighting function is used to provide more significance to input images with pixel values in the center of the function. Single-precision floating point values are used to encode recovered radiance map. The approach proposed by Mitsunaga and Nayar [8] utilizes polynomial approximation for their response function. This technique is suitable for low-cost consumer equipment. Several tone-mapping methods have been developed in the literature to convert real-world luminances into display luminances and meet the growing demand for displaying HDR data on conventional display devices. To achieve visually plausible results, most tone mapping techniques utilize photoreceptor adaptation [9]. The local light adaptation attribute of the Human Visual System (HVS) was implemented by a local operator to be in accordance with an observer's visual perception while seeing an input image, whereas a global operator is spatially invariant and less effective than a local operator.

Diatoms play a crucial function in the water quality monitoring process, and show nano- and micro-patterns. Due to the great diversity of species, manual analysis is impractical. Digital microscopes have been developed to investigate complicated patterns and to aid in the automatic examination and categorization of various specimens. Researchers have developed different imaging technologies for cell structure characterization [10]. When a specimen is illuminated and photographed using a digital microscope, only a small amount of apparent contrast and light is fully revealed from transparent cell walls of diatom [11]. Regions that are poorly illuminated in this case may seem underexposed whereas regions that are brightly illuminated may seem over exposed [12]. Therefore, in most situations, the whole luminance spectrum cannot be captured with one single shot. For this purpose, the specimen has to be photographed at various illumination levels to deal with the full spectrum of luminance variations. Singh et al. [13] performed multi-exposure image fusion for microscopic image data sets. This method utilizes the Weighted Least Squares (WLS) optimization technique for weighted average fusion. Multi-exposure image fusion has been proposed as a way to improve the contours and ornamentation features of diatom species. Recently, a new tonemapping method based on the Nonsubsampled contourlet transform (NSCT) was proposed to analyze multi-scale patterns in HDR images of diatom shells. [14]. For these reasons, the perfect combination of lighting and exposure values was discussed by Sánchez et al. [15]. Because the detailed structure

and ornamentation of frustules serves as the basis for diatom species classification, programmable lighting techniques and fusion are critical.

The exposure fusion is the alternative solution to HDR which fuses multi-exposure images into a single image. Over the years, various approaches to weighted average exposure fusion have been proposed. Among these, guided image filtering (GIF) [16] based on two-scale decomposition [17], global optimization using Generalized Random Walks (GRW) for fusion [18], fast exposure fusion (FEF) based on median filtering and recursive filtering (FEF) [19] approaches produce fusion results with better quality.

Orgden et al. [20] suggested an approach for the fusion of images based on pyramidal decomposition. The pyramidal decomposition is a multi-resolution drawing pad at increasingly fine precision to fill in the local spatial information. The Laplacian pyramid decomposes the input picture into separate spatial bands that are known to retain local spatial information as band-pass images [21]. Another multi-resolution fusion technique uses an input picture gradient map to generate a fused image with true information [22]. In such approach, the horizontal and vertical gradient maps are utilized to generate fused gradient maps. In the reconstruction process, this gradient fusion technique is based on the use of Discrete Wavelet Transform (DWT) and Quadrature Mirror Filters (QMFs).

Mertens et al. [23] suggested the Exposure Fusion (EF) technique utilizing a multi-resolution approach [21] without expanding the fused image's DR and tone-mapping. A multi-resolution approach was used in this process to merge input images, which is dependent on standard measurements such as saturation and contrast. Moreover, it was proposed that a flash picture could be included in a series of exposures to improve details in the fused image [23]. The efficiency of this multi-scale method depends on the amount of stages of decomposition, that is, the height of the pyramid. Bigger images would have to be processed in a higher number of pyramid levels than smaller images for better performance.

Compared to other established methods for exposure fusion, Kotwal and Chaudhuri [24] suggested a modern fusion alternative in which optimization techniques are used as an attempt to approximate the best matting feasible, which serves as weight for the purpose of fusion. Throughout this approach, a multi-objective cost function is built and uses the variational method to provide an iterative solution. At each iteration the matte is adaptively extracted from the data and the accompanying picture fused. Raman and Chaudhuri [25] published another matte-less approach, which used unconstrained optimization problems for the collection of locally high contrast pixels. In this paper, the use of a local information measure to regulate the details in the final fused image is described.

2. Problem formulation

The proposed multi-exposure image fusion approach is intended to take into consideration well-exposed portions of diatom pictures captured by microscopic imaging techniques. Some examples of multi-exposure data sets of different diatom species acquired by light microscopy and dark microscopy imaging techniques are shown in Fig. 1. All multi-exposure image stacks were photographed with a Canon EOS 1300D, 18MP Digital Single-Lens Reflex (DSLR) Camera mounted on a Brunel SP500, Objective × 60, NA 0.85.

The proposed method significantly enhances the quality of fused images, furthermore the output image can be seen directly on Low Dynamic Range (LDR) display devices without radiance domain restoration and tone manipulation [7]. In this paper, the input multi-exposure images used are perfectly aligned to avoid unwanted ghosting artifacts. Additionally, no post-processing is needed for the final synthesized image. As such, the approach discussed comprises the following main steps (See Fig. 2):
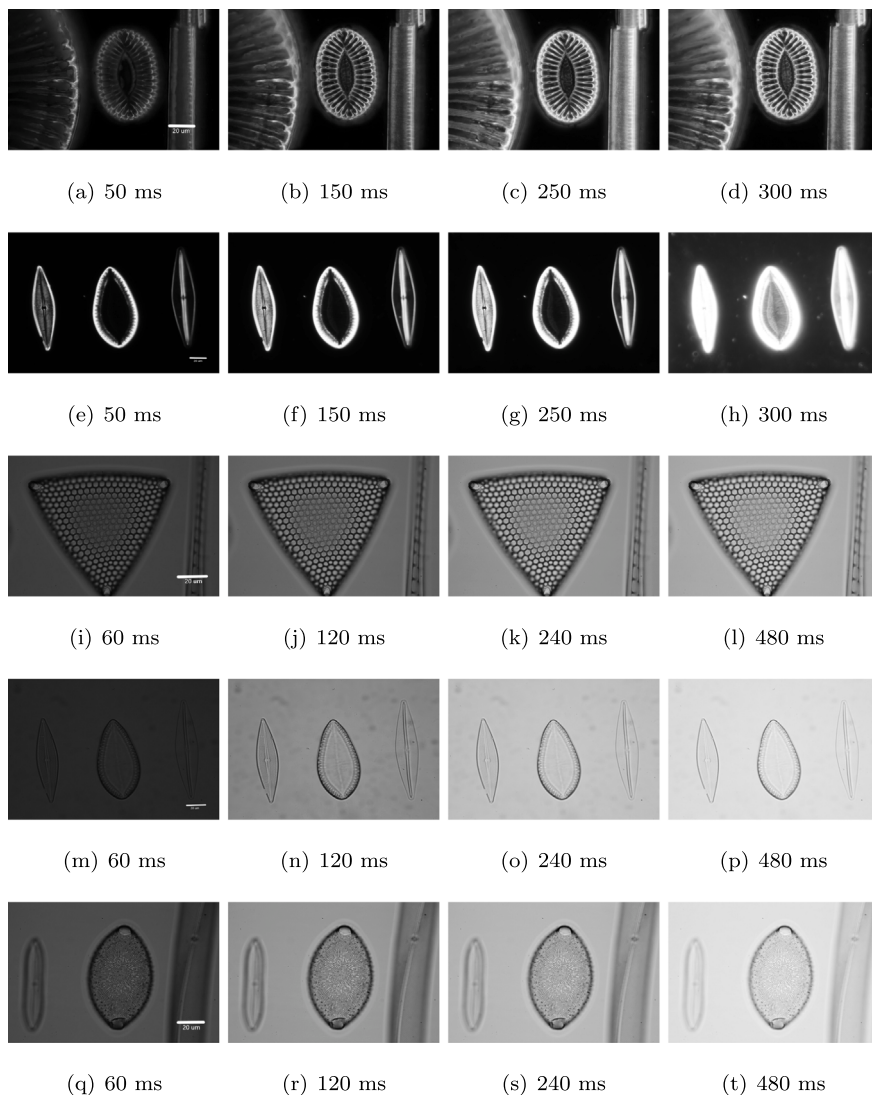
Fig. 1. Multi-exposure image series taken by light microscopy and dark microscopy imaging. (a–d) *Campylodiscus neofastuosus* (darkfield), (e–h) *Brachysira serians* (left), *Surirella peisonis* (center) and *Frustulia saxonica* (right) (darkfield), (i–l) *Triceratium favus* (brightfield), (m–p) *B. serians* (left), *S. peisonis* (center) and *F. saxonica* (right) (brightfield), (q–t) *Pleurosira laevis* (brightfield).

1. Non-parametric Modified Histogram Equalization (NMHE) is introduced to handle non-uniformity and non-cell regions across the input multi-exposure image.
2. A local measure of information which decides the contribution of pixels to the final fused images is proposed for weight map computation.
3. For seamless blending, multi-scale weighted average fusion based on pyramid decomposition is introduced.

3. Methodology

To overcome the limitations of a standard LDR digital camera which does not record full range of light variations present in HDR scenes, an intensity domain variation multi-exposure approach is proposed. Such limitations can be reduced by pre-processing the input multi-exposure images through histogram adjustment. Wu and Leou discuss this type of problem in [26], in which the Weighted Least Squares (WLS) based optimization solution is extended to input LDR images for information enhancement. Thus, to preserve the information available in the HDR scene's highly lighted and poorly illuminated regions, a pre-processing operator should be introduced before fusion. In the proposed

framework as shown in Fig. 2, a fusion method based on NMHE [27] has been considered here, in order to obtain an enhancement in the fused image with the minimum amount of noise.

Our approach is based on a pixel level fusion approach which combines information from different non-linearly transformed N exposures. The process of arithmetic combination is used to blend the corresponding pixels across input multi-exposure images. Arithmetic fusion for two input images can be summarized by the expression given as:

$$I_F(i,j) = W_1 \times I_1(i,j) + W_2 \times I_2(i,j) + C \tag{1}$$

where I_1, I_2, and I_F denotes the input multi-exposure images and blended output image respectively at location (i,j). W_1 and W_2 represent the weights computed across individual input images which control the contribution of input images in the fused image [28,29] and C the mean offset.

Computation of the mean image across input images constitutes an example of arithmetic fusion technique. The fused image is computed by taking the mean of input exposures; i.e., $W_1 = 1/2$, $W_2 = 1/2$ and $C = 0$. Despite being significantly more computationally efficient than most of other existing image fusion methods, a limited performance is achieved by image averaging and other arithmetic fusion techniques.
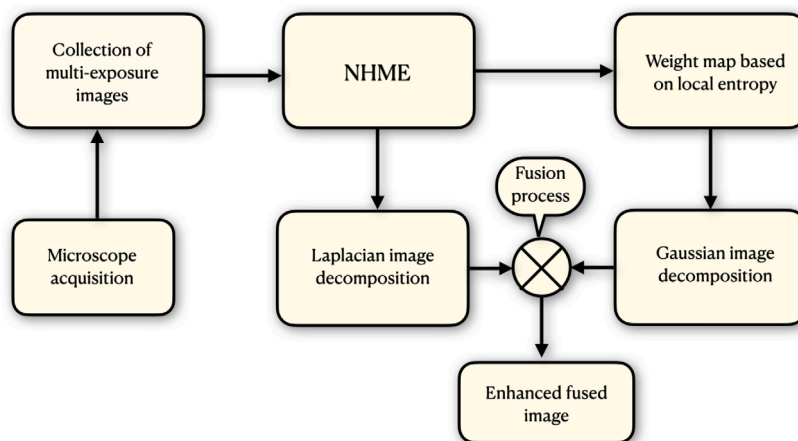
Fig. 2. Schematic of the proposed method of image fusion which uses NMHE as a pre-processing operator.
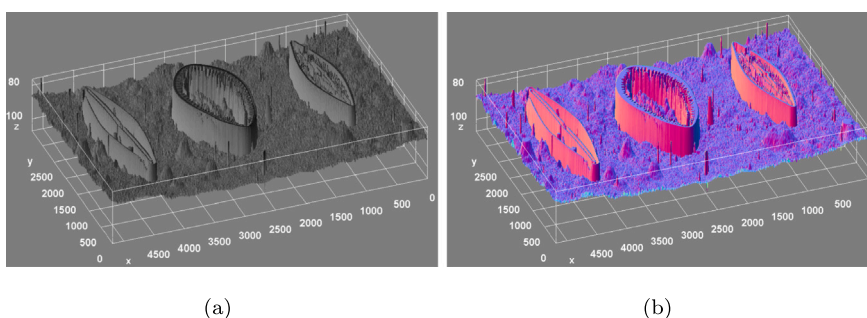

(a)

(b)

Fig. 3. Noise effect due to non-cell background region.(a) Surface plot of cell region and non-cell region of *C. neofastuosus* shown in Fig. 1(n); (b) Pseudocolor depiction of surface plot. Different colors are used to highlight relative fluctuations of pixel values in the cell region and non-cell region.

The key reason for this is the lack of color, arising from disruptive superposition while integrating input images. Furthermore, reduction of contrast is also introduced when a normalized sum is used, for example through the image averaging process. Calculation of a mean image generally yields reasonable image quality in areas where pixel values are identical, but the image quality is rapidly decreasing in regions where pixel values are completely different. The poorest results are obtained in places where pixel values are photographically opposite to each other in input exposures.

3.1. Pre-processing of microscopy multi-exposure images with histogram modification

In most cases, biologists adopt a fixed exposure setting based on their personal preferences to analyze the features of the cell under observation. Low contrast cell components are more difficult to analyze at short exposure values than bright cell parts that may be overexposed at a too long exposure setting. The multi-exposure image series in Fig. 1 leads us to consider collecting details from frustules with multi-scale patterns using variable exposure settings. Non-cell pixels, on the other hand, may show a substantial amount of noise as shown in Fig. 3(a). In Fig. 3(b), a pseudocolor plot reveals the background's hidden noise from the image for a better visualization of the pixels values fluctuations. Pixels from different cell images collected at various appropriate exposure levels are considered for the histogram modification in the suggested pre-processing technique.

A generic contrast enhancement algorithm is suggested by Poddar et al. [27] in which the parameter setting does not depend upon the dynamic range of input image and it does not require manual parameter tuning during histogram modification. Also, after enhancement it may well retain the histogram shape [30]. As a first step the spikes are

eliminated from the original histogram which improves details and overcomes the problem of noise amplification in the fused image. It further maintains the balance between contrast enhancement and a faithful depiction of the original color appearance in the fused image.

In NMHE, a modified histogram is produced by introducing only certain pixels with a two-lagged horizontal diversity higher than the threshold value. Fig. 4(a) shows a microscopy image with under-exposed regions, over-exposed regions and a large non-cell background region at nearly the same gray levels. A Histogram with horizontal diversity is shown in Fig. 4(b) in which pixel intensity values are not distributed evenly over the whole intensity range (0–255). A Modified histogram is formed with two-lagged difference (Fig. 4(c)) which has a greater magnitude than a particular threshold for each row m and each column n (i.e $|I[m, n] - I[m, n-2]| > threshold$). For efficient implementation on hardware, row-wise pixel processing architecture is used for horizontal contrast computation [31]. The modified histogram ($h_{new}(i)$) with conditional probability is given by

$$h_{new}(i) = p[i|C] \qquad (2)$$

where $p[i|C]$ denotes the probability of occurrence of pixels having ith gray value in a horizontal contrast variation (C). The event C deals with histogram spikes produced from non-cell background regions. Hence, histogram equalization on $h_{new}(i)$ rather than h improves the contrast rather than the noise. However, $h_{new}(i)$ only uses the dynamic range for pixels with a sufficient level of contrast to the surrounding areas.

The default value of C is set empirically to six, which gives adequate results for all image data sets. A unique parameter from the original histogram (h_i) is calculated for uniform distribution in modified histograms. A method of normalization is applied to the original histogram (h_i) and clipped at a particular height with a value of ($1/L$). The Probability Density Function (u) is given for uniform distribution as

$$u = ones(L, 1)/L \qquad (3)$$

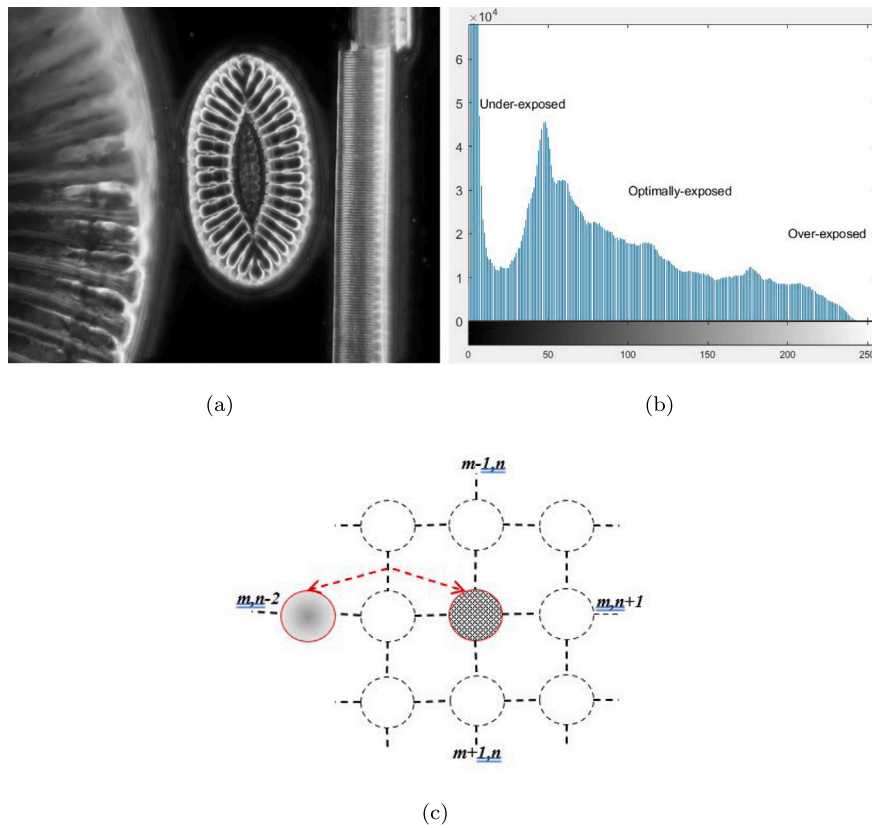(a)   (b)

(c)

Fig. 4. Histogram with horizontal diversity showing uneven tonal distribution and horizontal contrast computation. (a) Image captured at 300 ms; (b) Histogram and (c) Horizontal local contrast computation.

where $L = 256$ for an 8-bit gray scale image and the clipped histogram is given by

$$h_{new\,C}(n) = \begin{cases} (\frac{1}{L}), & \text{if } h_i(n) > (\frac{1}{L}) \\ h_i(n), & \text{if } h_i(n) \leq (\frac{1}{L}) \end{cases} \text{ for } n = 0, 1, \dots \dots L - 1 \quad (4)$$

A factor called un-equalization (Mu) which indicates the degree to which a uniform distribution does not match the original histogram is calculated as

$$Mu = sum(u - h_{new\,C}) \quad (5)$$

This factor (Mu) is utilized as weight factor for the calculation of modified Probability Density Function (PDF) which is given as

$$h_{NMHE} = (Mu)h_{new} + (1 - Mu)u \quad (6)$$

and the cumulative distribution function (CDF) of the image computed as

$$c_{NMHE}(n) = \sum_{i=0}^{n} h_{NMHE}(n) \quad (7)$$

The transfer function (T_{new}) to modify the histogram based on c_{NMHE} is defined as

$$T_{new}(n) = [(L - 1)c_{NMHE} + 0.5] \quad (8)$$

The enhanced output image is produced by using the following equation.

$$I(i, j) = \{T(S(i, j))| \forall S(i, j) \in S\} \quad (9)$$

where $S(i, j)$ is the source image and $I(i, j)$ represents the enhanced image.

The comparison between the original image histograms and the equalized images by applying four different techniques is shown in Fig. 5. We can note from Fig. 5(f) and 5(g), that NMHE preserves the

structure of the histogram. In addition, it does not add extra details to the input image. Figs. 5(a) and 5(b) show the original underexposed image and its NMHE corrected image, respectively. In Fig. 5(g), the variation in the histogram is moderated more accurately than in the other methods shown in 5(h,i,j).

In dark microscopy, the light impact can often arise from the peculiarity that the sensor exposure period is adjusted according to the light source. Fig. 1 shows how different the picture can appear based on the right combination of illumination and exposure time. A background correction is needed for microscopic images of diatoms to remove illumination defects such as shadows or dark areas. The enhancement based on Histogram Equalization (HE) [32], Brightness Preserving Bi-histogram Equalization (BBHE) [33] and Contrast Limited Adaptive Histogram Equalization (CLAHE) [34] introduces washed-out appearance and distortion which can be observed in Fig. 5(c–e). The default parameter values (number of tiles = [8 8], contrast enhancement limit=0.01, number of histogram bins = 256 and uniform distribution with $\alpha = 0.4$) suggested in [34] are utilized for assessing CLAHE's performance to make fair comparisons. However, NMHE can preserve the naturalness of the images and prevent amplification of the noise present in the background, which is clearly visible in Fig. 5(b).

The amount of noise amplification and distortion caused by the histogram modification approaches is also analyzed quantitatively. The 220 enhanced multi-exposure images of *Aqualitas dataset* [35] are compared based on Entropy (E) and Structural Similarity Index Measure (SSIM) to measure detail preservation and distortion introduction [36]. The SSIM between source $S(i, j)$ image and enhanced image $I(i, j)$ is defined by

$$SSIM(S, I) = \frac{(2\mu_S \mu_I + c_1)(2\sigma_{SI} + c_2)}{(\mu_S^2 + \mu_I^2 + c_1)(\sigma_S^2 + \sigma_I^2 + c_2)} \quad (10)$$

where μ_S and μ_I are the average of S and I, respectively, σ_S^2 is the variance of S, and σ_I^2 is the variance of I. σ_{SI} represents the co-variance
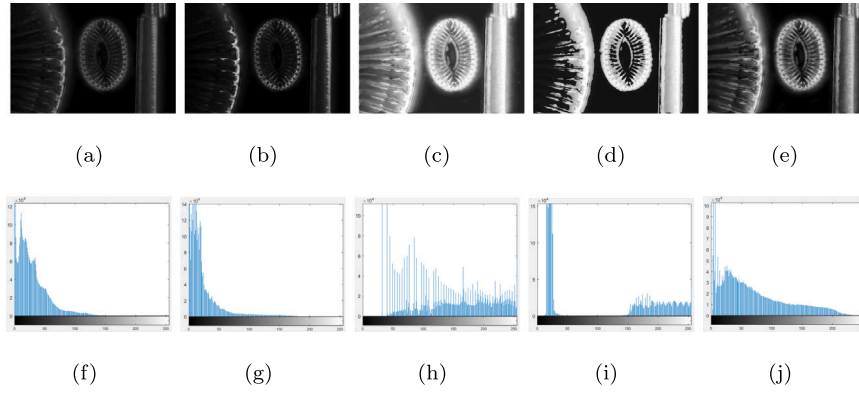
Fig. 5. Histogram of a multi-exposure image enhanced by different techniques.(a, f) Original Image and Histogram ; (b, g) Image modified by NMHE and Histogram. (c, h) Image modified by HE and Histogram; (d, i) Image modified by BBHE and Histogram; (e, j) Image modified by CLAHE and Histogram.
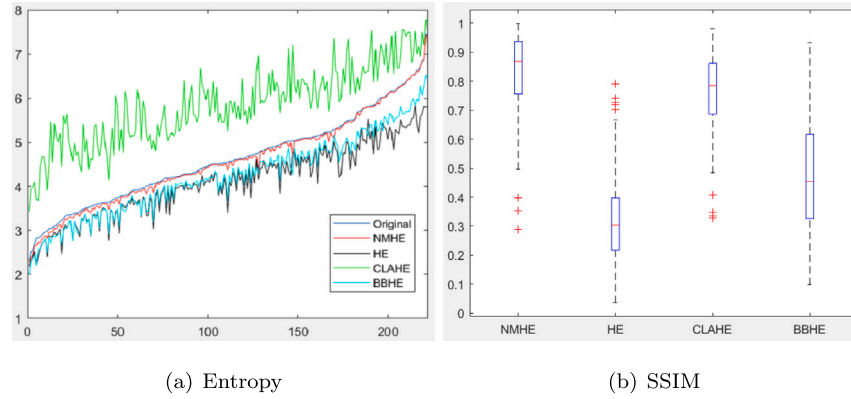

(a) Entropy

(b) SSIM

Fig. 6. Impact of histogram modification on *Aqualitas dataset* [35] multi-exposure microscopy image data set for 220 enhanced images by NMHE, HE, CLAHE and BBHE (a) Entropy results; (b) Box plot of SSIM index computed for 220 enhanced images.

of S and I and two constants c_1 and c_2 are used to stabilize the equation which depends on the dynamic range of image pixel-values.

It can be noticed from Fig. 6(a) that the entropy of enhanced multi-exposure images by NMHE remains closer or lower than that of the original multi-exposure images, which verifies that no additional information is ever added to the enhanced images. Entropy values were arranged in ascending order for better visualization. In comparison to CLAHE, which preserves entropy to a greater extent but introduces additional distortion, the picture transformed by the suggested methodology demonstrates a considerable preservation of entropy without the introduction of any new details.

Fig. 6(b) shows the SSIM results as a box plot for the images enhanced by different histogram modification methods. We can notice that NMHE has the highest SSIM values compared with HE, BBHE and CLAHE which clearly indicates that NMHE introduces less distortion in the 220 enhanced images. Thus, prior to image fusion, NMHE can be used to enhance multi-exposure microscopy images to reveal all appearance details of diatom species so that image fusion algorithms are not affected by the non-cell background pixels.

In order to quantify the degree of preservation of details and the image quality, two new metrics have been defined. Degree of Entropy Un-preservation (DEU) and Mean SSIM Distortion (MSSIMD) have been calculated to find the average difference in entropy and amount of distortion that is present in the enhanced image. The value of DEU and MSSIMD is given by Eqs. (11) and (12), respectively. The metric values calculated by applying Eqs. (11) and (12) are presented in Table 1. As shown in Table 1, the DEU value for NMHE is the lowest, indicating that the entropy of 220 enhanced images is preserved even after histogram modification. This arises because, unlike HE, BBHE, and CLAHE, NMHE does not add any new information in the process

Table 1
Quantitative analysis on *Aqualitas* image dataset [35] multi-exposure microscopy image data set for 220 enhanced images by applying NMHE, HE, CLAHE and BBHE methods.

Metric	NMHE	HE	BBHE	CLAHE
DEU	**0.0495**	0.5174	1.2271	0.3976
MSSIMD	**0.1702**	0.6842	0.2406	0.5302

of histogram modification. In comparison to HE, BBHE, and CLAHE, we can notice from Table 1 that NMHE has the lowest MSSIMD value, suggesting minimal structural change in the enhanced image.

$$DEU = \frac{\sum_{k=1}^{N} |E(S_k) - E(I_k)|}{N} \tag{11}$$

$$MSSIMD = \frac{(220 - \sum_{k=1}^{N} SSIM(I_k))}{N} \tag{12}$$

3.2. Local entropy and weight map computation

In this approach local entropy it is utilized for weight map computation. It is used to analyze the randomness present in the source images. It can be defined as:

$$H = -\sum_{G=0}^{255} P(G) log_2(P(G)) \tag{13}$$

where $P(G)$ is the likelihood of the intensity value G. In our case, this local measure is considered as a metric of information gained within the local window for the computation of weight function.

In our multi-exposure image fusion approach, the local Entropy is varying across input images photographed at different exposure values.
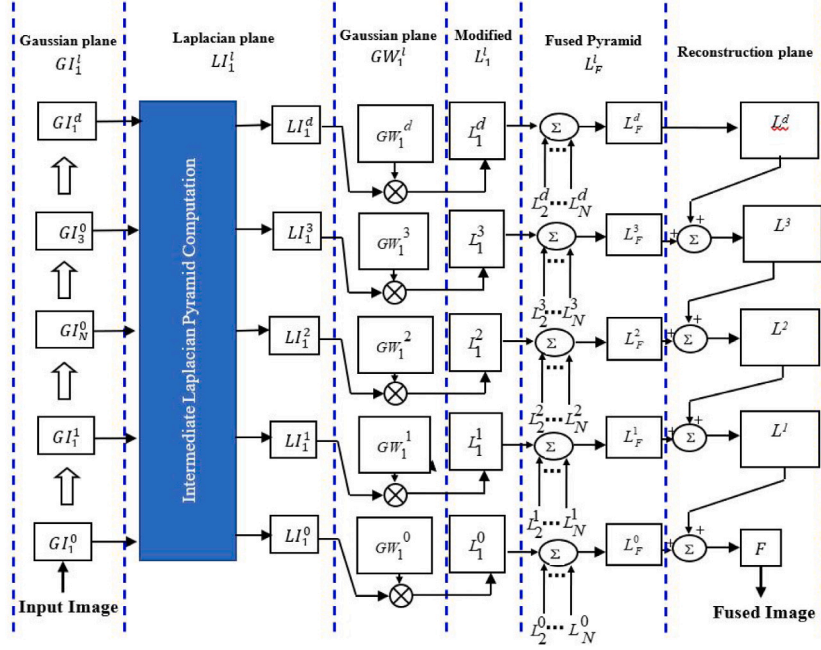
Fig. 7. Manipulation of spatial frequency bands and fusion: illustrating the conceptual framework of detail-enhanced image fusion in local Laplacian domain. For the sake of simplicity, we have generated the Laplacian pyramid (L_1^l) of single input image and Gaussian pyramid (GW_1^l) of the corresponding weight map function. Where $L_2^0, L_3^0 \ldots \ldots L_N^0$ are the modified Laplacian pyramids of level zero computed across all of the input images.

Well-exposed regions give higher local entropy values relative to the shadows and highlights. To compute local entropy, the input image is divided into small blocks of window size 3×3. The local entropy for the kth input image within 3×3 local windows k' is computed as follows:

$$H_{i,j,k} = -\sum_{G=0}^{255} P_{i,j,k}(G) log_2(P_{i,j,k}(G)) \qquad (14)$$

$$W_{i,j,k} = \left[\sum_{k'=0}^{N} H_{i,j,k'} \right]^{-1} \times H_{i,j,k'} \qquad (15)$$

where $H_{i,j,k}$ represents the entropy value computed in each block and $W_{i,j,k}$ denotes entropy's normalized value, which is serving as a weight map function to regulate pixel contribution at ij^{th} position in kth image.

3.3. Pyramid generation and image fusion

Researchers have employed multi-resolution techniques to fuse and modify details at many scales in recent years, overcoming the problem of seam and contrast reversal artifact caused during the image fusion process [20]. In the present approach, the input images have been decomposed into various spatial bands through a Laplacian pyramid and manipulated based on a local entropy measure. In the final fused image, only the local regions which have maximum information contribute further. A high entropy value suggests that the picture block in the source image has a higher weight throughout the fusion process. For edge-aware smoothing, a simple threshold was proposed by Paris et al. [37] to differentiate edge-detail from small-scale details. In a similar spirit, we use thresholding to enhance the Laplacian pyramid before using the Gaussian pyramid of local entropy to manipulate it. The proposed detail-enhanced fusion algorithm in multi-resolution domain is shown in Fig. 7.

Given an input image I_k, a low pass filtered image is created by convolving original image $GI_k^0 = I_k$ with the Gaussian kernel. Sub-sampling is used to build the next level GI_k^1 by eliminating every other pixel and row from the filtered picture. By repeating this process several times, we may create a Gaussian pyramid, which is a stack of reduced

resolution images $GI_k^0, GI_k^1, GI_k^2, \ldots, GI_k^d$. For levels $0 < l < d$, the l_{th} Gaussian level for k_{th} image is given by

$$GI_k^l(i,j) = \sum_m \sum_n w(m,n) GI_k^{l-1}(2i+m, 2j+n), \qquad (16)$$

where $w(\bullet)$ is the equivalent weighting function, which is separable: $w(m,n) = w(m)w(n)$. For more details, readers are suggested to see [20]. The number of decomposition levels in the proposed fusion technique is determined by the size of the input image, and the possible number of levels for pyramid decomposition is given by

$$d = \left\lfloor \frac{log(min(r,c))}{log(2)} \right\rfloor \qquad (17)$$

where $\lfloor \bullet \rfloor$ is the floor operator, and r and c are the number of rows and number of columns in the input image.

For detail enhancement, a point-wise nonlinearity function $r(\bullet)$ is derived from $g = GI_k^l(i,j)$ at each position (i,j). Where, g is the coefficient of the Gaussian pyramid at (l,i,j) to build Laplacian pyramid ($LI_{i,j,k}^l$) of transformed image at that level. For instance, to enhance details, a local S-shaped tone curve centered on g is applied. The remapping function proposed in [37] is used to separate details from edges, which is given by

$$\begin{cases} g + sign(i-g)\sigma_r(|i-g|/\sigma_r)^\alpha & \text{if } i \leq \sigma_r \\ g + sign(i-g)(\beta(|i-g|/\sigma_r) + \sigma_r) & \text{if } i > \sigma_r \end{cases} \qquad (18)$$

where α, β and σ_r are the user defined parameters that serve as detail enhancement thresholds. In the proposed fusion approach, we set $\alpha = 0.15$, $\beta = 1$ and $\sigma_r = 0.12$ to produce Laplacian pyramid for details enhancement.

Gaussian pyramid of local entropy controls the pixel contribution from multiple exposures that yields the modified Laplacian pyramid L^l, which provides the fused Laplacian pyramid and is given by

$$L_F^l = \sum_{k=1}^{N} LI_{i,j,k}^l \times GW_{i,j,k}^l \qquad (19)$$

where $LI_{i,j,k}^l$ denotes the Laplacian pyramid of input images after enhancement and $GW_{i,j,k}^l$ represents the Gaussian pyramid of scalar weight maps calculated by Eq. (15). In the same way that we computed
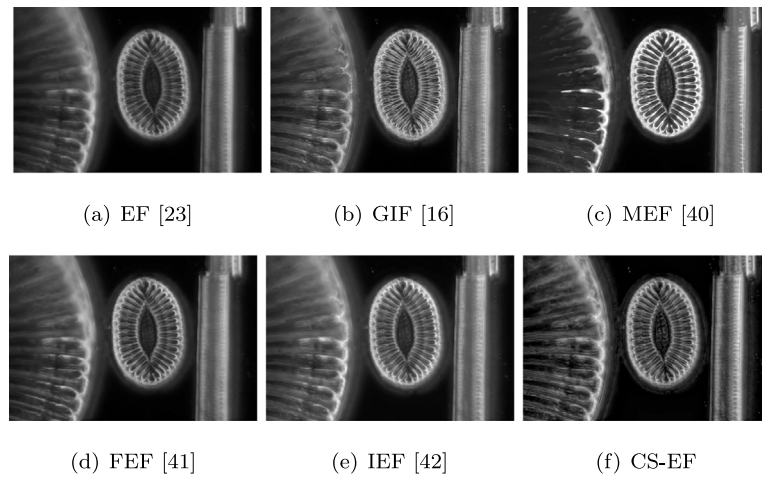
(a) EF [23] (b) GIF [16] (c) MEF [40]

(d) FEF [41] (e) IEF [42] (f) CS-EF

Fig. 8. Comparison of the five existing image fusion algorithms and CS-EF using the *C. neofastuosus* images acquired by darkfield microscopy.

the Gaussian pyramid of the input picture in Eq. (16), we compute the Gaussian pyramid of the weight map function. The well exposed detailed enhanced fused image is reconstructed from each enhanced fused Laplacian pyramid L_F^l by expanding and summing up each enhanced level, which is given by

$$F = L_F^0(i,j) + L_F^2(i,j) + L_F^3(i,j) + \cdots \ldots L_F^d(i,j) \qquad (20)$$

4. Results and discussion

The multi-exposure image fusion method described in this paper is implemented on MATLAB-2018a. The results generated from the proposed approach yields natural contrast in output fused images. The method is tested on different microscopic image data sets that are captured at different exposure levels using darkfield and lightfield microscopy techniques. The fusion quality is assessed using different standard quality metrics, such as $Q^{AB/F}$, $L^{AB/F}$, $N^{AB/F}$, Q^{SF}, Q^{AG} [38, 39] to test the validity of the present approach.

In Figs. 8, 9, 10, 11 and 12, we compare our fusion results with five state-of-the-art image fusion methods that including EF [23], GIF [16], Matting based Exposure Fusion (MEF) [40], FEF [41] and Illumination estimation based Exposure Fusion (IEF) [42]. Fig. 8(a–f) and Fig. 9(a–f) illustrate the fusion results for *C. neofastuosus* and *B. serians* (left), *S. peisonis* (center) and *F. saxonica* (right) image data sets acquired by dark microscopy imaging. We can observe that the CS-EF results shown in Fig. 8(f) and 9(f) preserve details in fine micro-structures within the specimen without blooming artifacts seen on the transparent regions illuminated by the light source. Moreover, the CS-EF significantly reduces the glare caused by brighter regions across boundaries as compared to results produced by EF, GFF, MEF, FEF and IEF.

In Figs. 10 and 11, we show the qualitative comparison between CS-EF and other methods for *T. favus*, and *B. serians* (left), *S. peisonis* (center) and *F. saxonica* (right) image data sets acquired by brightfield microscopy imaging. The results of CS-EF are illustrated in Fig. 10(f) and Fig. 11(f). As we observe from fusion results of CS-EF, the proposed method is able to preserve details in cell-region while the background noise is reduced gradually. It is observed from Fig. 10(f) that the complete light variations are preserved accurately without producing any artifacts. Throughout this way the detail information can be discovered in the cell-regions, particularly when using multi-exposure microscopy imaging techniques.

The results produced by the different multi-exposure fusion techniques including EF, GIF, MEF, FEF, IEF and CS-EF for *P. laevis* are shown in Fig. 12. The CS-EF results in Fig. 12(f)) reveal that details in diatom species' well-exposed areas are preserved, and the fused image preserves sharpness of the fine micro-structures within the specimen.

So the information collected under various reflections or absorptions is retained in the fused image. Here we report that the CS-EF improves local contrast of the blended image and also eliminates the noise present in the homogeneous areas. Therefore, the proposed fusion method is less prone to be noisy in non-cell pixels that are present in the background and produces better results than existing state-of-the-art fusion methods.

To test the performances of the proposed fusion method, it has also been tested on the color image datasets. In our implementation, we have tested our fusion approach on the micrographs of blood samples captured using darkfield microscopy. The multi-exposure images shown in Figs. 13(a–d) show the fact that the morphology of erythrocytes [43] cannot be captured with a single shot. Blood samples must be photographed using a variety of exposure settings, and image fusion can then be used to improve details. As it can be observed from the fusion results shown in Fig. 13(j), CS-EF depicts significant improvement in the details as compared with other methods shown in Figs. 13(e–i). Moreover, it seems to preserve color information present in the input images. The full resolution images of fusion results shown in Figs. 8–13 can be found on the web link https://doi.org/10.6084/m9.figshare.14854161.v8. Apart from them, the supplementary material contains more fusion results which support the reported results.

The performance of the experiments is quantitatively assessed to determine the efficiency of the fusion processes. Five common image fusion quality metrics were considered for objective evaluation (see Table 2). The goal is to assess the fusion output from different viewpoints, such as the amount of details transferred from source images to the blended picture $Q^{AB/F}$ [38], total lack of information in the fused image $L^{AB/F}$ [39] and artifacts added to the fused image by fusion process $N^{AB/F}$ [39]. $Q^{AB/F}$ is a gradient-based fusion consistency metric that calculates the quantity of edge information transmitted to the blended picture from the inputs. Q^{SF} originates from the human visual system (HVS) and shows the average degree of operation in picture [44]. The Q^{SF} is defined as

$$Q^{SF} = \sqrt{R_f^2 + C_f^2} \qquad (21)$$

where R_f^2 refers to the measured spatial frequencies from pixels in row and C_f^2 refers to the measured spatial frequencies from pixels in column [44].

Q^{AG} evaluates the amount of clarity and sharpness of the image fused from the source images, which is measured as

$$Q^{AG} = \frac{\sum_i \sum_j ((F(i,j) - F(i+1,j))^2 + (F(i,j) - F(i,j+1))^2)^{1/2}}{mn} \qquad (22)$$

where F is the fused image. Ultimately we want a successful picture fusion process to produce a higher Q^{AG} value.

(a) EF [23] (b) GIF [16] (c) MEF [40]

(d) FEF [41] (e) IEF [42] (f) CS-EF

Fig. 9. Comparison of the five existing image fusion algorithms and CS-EF using the *B. serians* (left), *S. peisonis* (center) and *F. saxonica* (right) images acquired by darkfield microscopy.

(a) EF [23] (b) GIF [16] (c) MEF [40]

(d) FEF [41] (e) IEF [42] (f) CS-EF

Fig. 10. Comparison of the five existing image fusion algorithms and CS-EF using the *T. favus* images acquired by brightfield microscopy.

(a) EF [23] (b) GIF [16] (c) MEF [40]
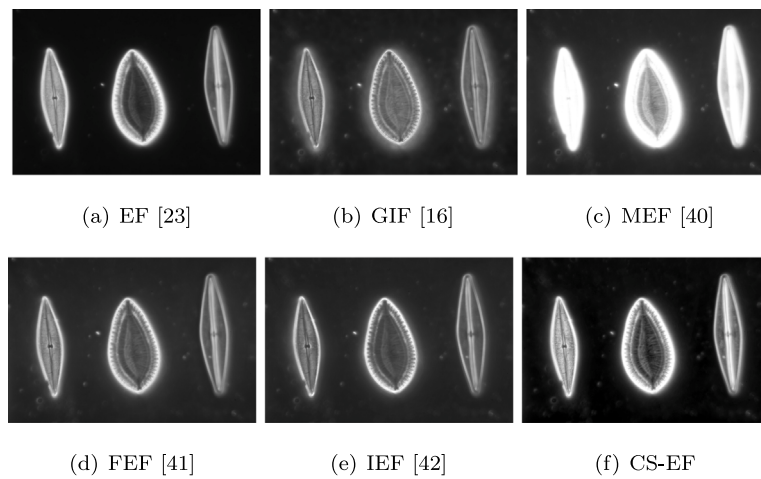
(d) FEF [41] (e) IEF [42] (f) CS-EF

Fig. 11. Comparison of the five existing image fusion algorithms and CS-EF using the *B. serians* (left), *S. peisonis* (center) and *F. saxonica* (right) images acquired by brightfield microscopy.
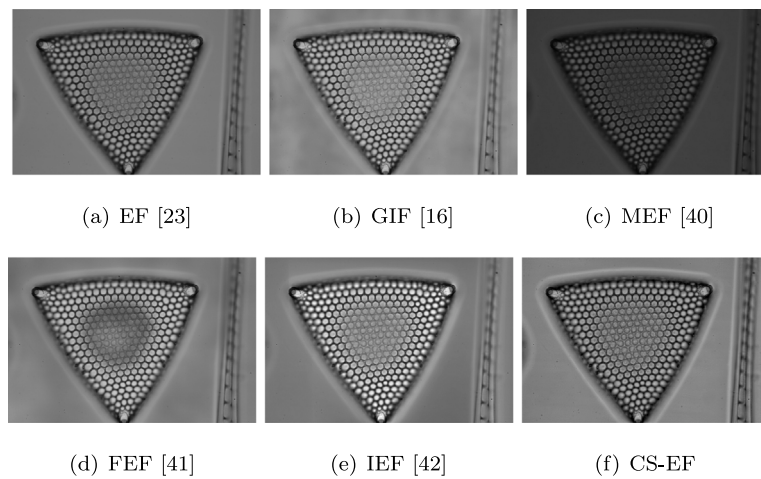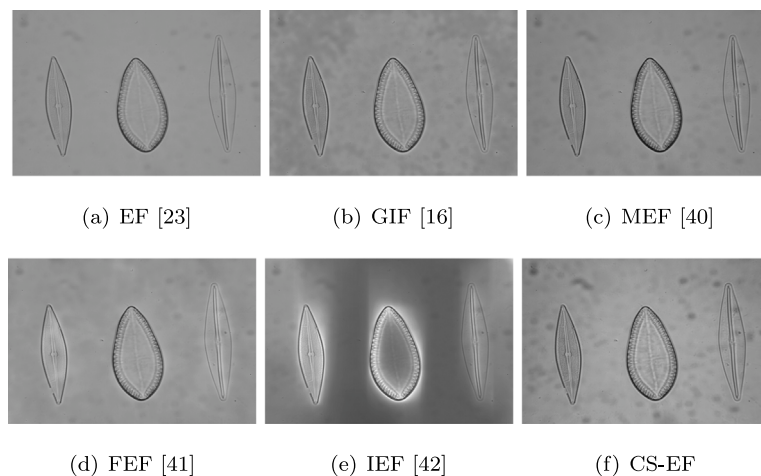
In Table 2, the metric values computed from the fusion results of EF, GIF, MEF, FEF, IEF and CS-EF are presented, depicting better values in bold. Fused picture with better quality would yield the highest $Q^{AB/F}$ value. By comparison, the lower the $N^{AB/F}$ and $L^{AB/F}$ values, the better the composite picture quality. In terms of non-reference quality metrics such as Q^{SF} and Q^{AG}, higher scores are expected from the ideal fusion method. The objective assessments presented in Table 2 show that on three data sets the CS-EF outperformed the other methods in
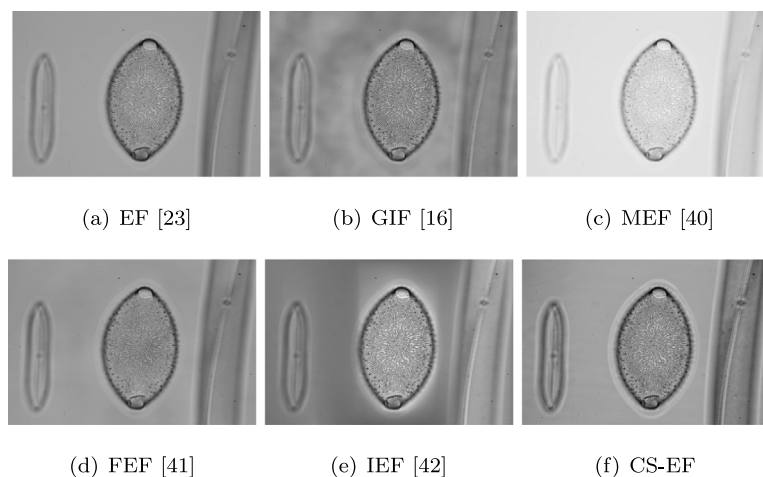
(a) EF [23] (b) GIF [16] (c) MEF [40]

(d) FEF [41] (e) IEF [42] (f) CS-EF

Fig. 12. Comparison of the five existing image fusion algorithms and CS-EF using the *P. laevis* images acquired by brightfield microscopy.

(a) 50 ms (b) 150 ms (c) 250 ms (d) 300 ms

(e) EF [23] (f) GIF [16] (g) MEF [40]

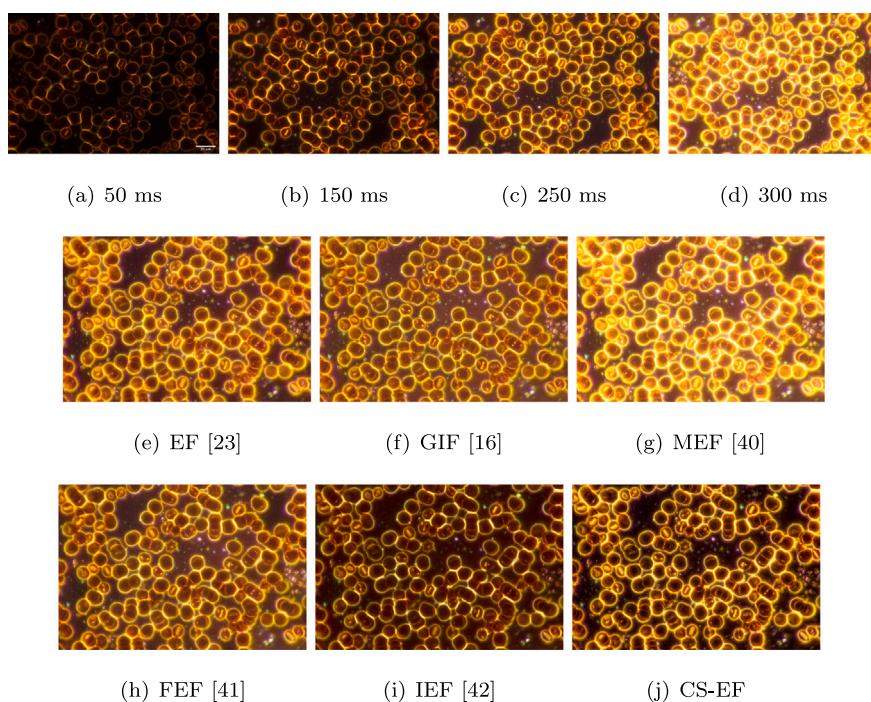(h) FEF [41] (i) IEF [42] (j) CS-EF

Fig. 13. Extension to color image data set. (a–d) Four multiexposure input images; (e–j) Comparison of the five existing image fusion algorithms and CS-EF using *RAT-blood* images acquired by darkfield microscopy.

terms of $Q^{AB/F}$, $L^{AB/F}$ Q^{SF} and Q^{AG} metrics for *T. favus*, *B. serians* (brightfield) et al. and *RAT-blood* image data sets, depicting also better edge preservation ability. It can be noticed that CS-EF yields better $Q^{AB/F}$, Q^{SF}, and Q^{AG} values, for two data sets which include *B. serians (darkfield)* et al. and *P. laevis*. Therefore, better edge details are present in the fused images with lesser background noise which can help in identifying the species based on image analysis techniques [12]. The smaller value of $L^{AB/F}$ for *P. laevis* indicates that CS-EF introduces less noise than other methods. We can notice that CS-EF does not perform better in terms of $Q^{AB/F}$ and $L^{AB/F}$ for *C. neofastuosus*. For *C. neofastuosus* image data set, GIF has performed well in terms of $Q^{AB/F}$ and $L^{AB/F}$, and CS-EF outperforms the runner-greatest score. GIF has also outperformed in terms of $L^{AB/F}$ for *T. favus* dataset.

On the other hand, EF had outperformed well in terms of $N^{AB/F}$ with a trade-off in terms of edge-preservation capability for the *T. favus* data set. Aside from the three image data sets, MEF produces lower $N^{AB/F}$ values for *B. serians(brightfield)* et al. *C. neofastuosus*

and *RAT-blood* data sets. It also outperforms in terms of $L^{AB/F}$ for *B. serians (darkfield)* et al. datasets. Based on our findings, the histogram adjustment operation performed prior to the fusion procedure aids in the production of high-quality fused images from multi-exposure picture series of the same specimen. As a result, when NMHE is utilized as a pre-processing tool before fusion, CS-EF fusion techniques excel in enhancing delicate microstructures within specimens. Overall, the suggested approach introduces less distortion while preserving considerable edge features in the fused picture.

For the 20 microscopy data sets, Table 3 shows the average values for each quality metric for the proposed approach and current state-of-the-art methods. For all 20 image datasets, the proposed method yields the best average values for all quality measures except $N^{AB/F}$. We can notice that MEF performs better in terms of $N^{AB/F}$, which offers the lowest average value for 20 image data sets fusion results. This implies that the proposed technique's fused image incorporates more significant and accurate information from the input source data.

Table 2
Comprehensive quantitative analysis of multi-exposure image fusion results obtained from 6 microscopy data sets.

Image	Metric	EF	IEF	FEF	MEF	GIF	CS-EF
C. neofastuosus	$Q^{AB/F}$	0.48	0.50	0.50	0.57	**0.71**	0.6
	$L^{AB/F}$	0.46	0.40	0.38	0.38	**0.18**	0.34
	$N^{AB/F}$	0.06	0.10	0.12	**0.05**	0.11	0.06
	Q^{SF}	1.96	2.48	2.40	4.28	3.89	**5.6**
	Q^{AG}	0.82	1.06	1.00	1.51	1.57	**2.4**
T. favus	$Q^{AB/F}$	0.92	0.90	0.93	0.52	0.91	**0.94**
	$L^{AB/F}$	0.07	0.03	0.04	0.42	0.06	**0.03**
	$N^{AB/F}$	**0.01**	0.06	0.03	0.06	0.02	0.03
	Q^{SF}	2.99	4.05	3.57	1.81	3.49	**4.8**
	Q^{AG}	1.12	1.59	1.32	0.66	1.43	**2.26**
B. serians (darkfield)	$Q^{AB/F}$	0.57	0.62	0.70	0.64	0.69	**0.82**
	$L^{AB/F}$	0.37	0.16	0.14	**0.14**	0.23	0.16
	$N^{AB/F}$	0.06	0.22	0.16	0.22	0.08	**0.02**
	Q^{SF}	1.04	1.57	1.61	1.69	1.70	**3.12**
	Q^{AG}	0.29	0.48	0.61	0.64	0.65	**1.31**
P. laevis	$Q^{AB/F}$	0.48	0.61	0.60	0.60	0.62	**0.89**
	$L^{AB/F}$	0.45	0.14	0.13	0.25	**0.03**	0.04
	$N^{AB/F}$	0.08	0.25	0.27	0.16	0.35	**0.07**
	Q^{SF}	2.97	4.48	2.81	2.62	3.73	**5.21**
	Q^{AG}	0.96	1.30	1.21	1.10	1.33	**2.26**
B. serians (brightfield)	$Q^{AB/F}$	0.56	0.69	0.72	0.68	0.72	**0.89**
	$L^{AB/F}$	0.39	0.11	0.12	0.30	0.22	**0.05**
	$N^{AB/F}$	0.05	0.20	0.16	**0.01**	0.05	0.06
	Q^{SF}	0.92	1.39	0.95	0.75	1.19	**3.74**
	Q^{AG}	0.29	0.43	0.41	0.34	0.46	**1.61**
RAT-blood	$Q^{AB/F}$	0.31	0.25	0.28	0.31	0.29	**0.35**
	$L^{AB/F}$	0.57	0.62	0.59	0.58	0.58	**0.42**
	$N^{AB/F}$	0.12	0.13	0.12	**0.11**	0.13	0.22
	Q^{SF}	3.87	4.18	3.78	3.59	4.07	**5.54**
	Q^{AG}	2.01	1.97	1.91	1.81	2.02	**2.95**

Table 3
Average value computed from quantitative analysis of multi-exposure image fusion results obtained from 20 microscopy data sets.

Metric	EF	IEF	FEF	MEF	GIF	CS-EF
$Q^{AB/F}$	0.766	0.751	0.0.760	0.707	0.796	**0.852**
$L^{AB/F}$	0.162	0.160	0.161	0.237	0.129	**0.104**
$N^{AB/F}$	0.073	0.091	0.078	**0.038**	0.071	0.044
Q^{SF}	3.038	3.529	2.976	3.336	3.546	**4.846**
Q^{AG}	0.996	1.147	1.004	1.085	1.212	**2.077**

Therefore, the current image fusion method outperforms alternative methods, according to this study.

5. Conclusion

A Multi-exposure image fusion method is described to preserve under-exposed and overexposed regions in microscopy. In the present approach a local entropy measure is utilized for computing weight map function. A modified Laplacian pyramid is computed based on this weight map function to build a fused image across the input data. NMHE is also shown to be a good pre-processing operator for dealing with background noise in non-cell regions and avoiding inconsistencies between input multi-exposure images used in the fusion process.

Diatoms are microscopic algae with a great range of contrast and brightness, in particular with observations performed utilizing dark field and bright field illumination. Due to high dynamic range of contrast and brightness, a single image of the diatom cannot be produced with all the important details inside the bright and dark regions. The main goal of exposure fusion is to reconstruct the fused image that shows far greater detail than any image in the original sequence. When the specimen is photographed with variable exposure values, the clarity of the optical presentation can be maximized using the image fusion. Standard multi-exposure techniques are commonly used with the purpose of improving the details in the fused image. However, the

quality of the multi-exposure image input stack determines the fusion method's outcome. The fusion method presented in this study helps to improve the information found inside the specimen under examination utilizing dark-field or bright-field microscopy. Of course, pre-processing of the input multi-exposure image series is an excellent tool to increase the features with the purpose of reducing the classification error of different diatom species. Although, employing a modern darfikeld microscopy technique with a perfect combination of illumination and exposure value, the quality of the fused image can still be improved. In order to capture the details of a transparent 3D specimen, one can take into account superimposed darkfield microscopy [11] in which, for example epi-illumination and mirrored lenses are used. Furthermore, modern methods of dark-field microscopy may often be utilized where objects are lit with light of various wavelengths so that sequences of images are obtained. As a further research, the approaches described in this study can be extended to other microscopic modalities such as phase contrast or differential interference contrast (DIC) for improving the final result.

Declaration of competing interest

The authors declare that they have no known competing financial interests or personal relationships that could have appeared to influence the work reported in this paper.

References

[1] J. Piper, in: G. Cristobal, S. Blanco, G. Bueno (Eds.), Light Filtering in Microscopy, Modern Trends in Diatom Identification: Fundamentals and Applications, Springer International Publishing, 2020, pp. 95–111.

[2] A. Pedraza, G. Bueno, Ó. Déniz, G. Cristóbal, S. Blanco, M. Borrego-Ramos, Automated diatom classification (part b): A deep learning approach, Appl. Sci. 7 (2017) 460.

[3] B.J. Chang, K. Winick, Silver-halide gelatin holograms, in: T.C. Lee, P.N. Tamura (Eds.), Recent Advances in Holography, in: Society of Photo-Optical Instrumentation Engineers (SPIE) Conference Series, vol. 215, 1980, pp. 172–177.

[4] F. Kienberger, V. Pastushenko, G. Kada, T. Puntheeranurak, L. Chtcheglova, C. Riethmueller, C. Rankl, A. Ebner, P. Hinterdorfer, Improving the contrast of topographical afm images by a simple averaging filter, Ultramicroscopy 106 (8) (2006) 822–828.

[5] J. Spiegelberg, J.C. Idrobo, A. Herklotz, T.Z. Ward, W. Zhou, J. Rusz, Local low rank denoising for enhanced atomic resolution imaging, Ultramicroscopy 187 (2018) 34–42.

[6] C. Vinegoni, C.L. Swisher, P.F. Feruglio1, R. Giedt, D. Rousso, S. Stapleton, R. Weissleder, Real-time high dynamic range laser scanning microscopy, Nat. Commun. 7 (2016) 1–13.

[7] P.E. Debevec, J. Malik, Recovering high dynamic range radiance maps from photographs, in: Proceedings of the 24th Annual Conference on Computer Graphics and Interactive Techniques, SIGGRAPH '97, ACM Press/Addison-Wesley Publishing Co., USA, 1997, pp. 369–378.

[8] S. Nayar, T. Mitsunaga, High dynamic range imaging: spatially varying pixel exposures, in: Proceedings IEEE Conference on Computer Vision and Pattern Recognition. CVPR 2000 (Cat. No. PR00662) vol. 1, 2000, pp. 472–479.

[9] M.H. Kim, T. Weyrich, J. Kautz, Modeling human color perception under extended luminance levels, ACM Trans. Graph. 28 (3).

[10] P. Gröger, N. Poulsen, J. Klemm, N. Kröger, M. Schlierf, Establishing super-resolution imaging for proteins in diatom biosilica, Sci. Rep. 6 (1) (2016) 36824, http://dx.doi.org/10.1038/srep36824.

[11] J. Piper, Image processing for the optimization of dynamic range and ultra-high contrast amplification in photomicrography, in: Modern Research and Educational Topics in Microscopy, Formatex Research Center, Badajoz, Spain, 2010, pp. 1436–1444.

[12] Z. Yin, H. Su, E. Ker, M. Li, H. Li, Cell-sensitive phase contrast microscopy imaging by multiple exposures, Med. Image Anal. 25 (1) (2015) 111–121.

[13] H. Singh, G. Cristóbal, V. Kumar, Multifocus and multiexposure techniques, in: Modern Trends in Diatom Identification: Fundamentals and Applications, Springer International Publishing, Switzerland, 2020, pp. 165–181.

[14] H. Singh, G. Cristóbal, S. Blanco, G. Bueno, C. Sánchez, Nonsubsampled contourlet transform based tone mapping operator to optimize the dynamic range of diatom shells, Microsc. Res. Tech. (2021) 1–12.

[15] C. Sánchez, J. Ruiz-Santaquiteria Alegre, J. Espinosa Aranda, J. Salido, Automatization techniques. Slide scanning, in: Modern Trends in Diatom Identification: Fundamentals and Applications, Springer International Publishing, Cham, 2020, pp. 113–131.

[16] K. He, J. Sun, X. Tang, Guided image filtering, IEEE Trans. Pattern Anal. Mach. Intell. 35 (6) (2013) 1397–1409.

[17] H. Singh, Detail enhanced multi-exposure image fusion based on edge preserving filters, ELCVIA Electr. Lett. Comput. Vis. Image Anal. 16 (2) (2018) 13–16.

[18] R. Shen, I. Cheng, J. Shi, A. Basu, Generalized random walks for fusion of multi-exposure images, IEEE Trans. Image Process. 20 (12) (2011) 3634–3646.

[19] S. Li, X. Kang, Fast multi-exposure image fusion with median filter and recursive filter, IEEE Trans. Consum. Electron. 58 (2) (2012) 626–632.

[20] J.M. Ogden, E.H. Adelson, J.R. Bergen, P. Burt, Pyramid-based computer graphics, RCA Engineer, pp. 30–5.

[21] P. Burt, E. Adelson, The laplacian pyramid as a compact image code, IEEE Trans. Commun. 31 (4) (1983) 532–540.

[22] V.S. Petrovic, C.S. Xydeas, Gradient-based multiresolution image fusion, IEEE Trans. Image Process. 13 (2) (2004) 228–237.

[23] T. Mertens, J. Kautz, F. Van Reeth, Exposure fusion: A simple and practical alternative to high dynamic range photography, Comput. Graph. Forum 28 (1) (2009) 161–171.

[24] K. Kotwal, S. Chaudhuri, An optimization-based approach to fusion of multi-exposure, low dynamic range images, in: 14th International Conference on Information Fusion, 2011, pp. 1–7.

[25] S. Raman, S. Chaudhuri, A matte-less, variational approach to automatic scene compositing, in: 2007 IEEE 11th International Conference on Computer Vision, 2007, pp. 1–6.

[26] Y. Wu, J. Leou, Multiexposure image fusion for dynamic scenes, in: 2017 40th International Conference on Telecommunications and Signal Processing, (TSP), 2017, pp. 544–547.

[27] S. Poddar, S. Tewary, D. Sharma, V. Karar, A. Ghosh, S.K. Pal, Non-parametric modified histogram equalisation for contrast enhancement, IET Image Process. 7 (7) (2013) 641–652.

[28] H. Singh, V. Kumar, S. Bhooshan, A novel approach for detail-enhanced exposure fusion using guided filter, Sci. World J. 2014 (2014) 1–8, http://dx.doi.org/10.1155/2014/659217.

[29] H. Singh, V. Kumar, S. Bhooshan, Weighted least squares based detail enhanced exposure fusion, ISRN Sig. Process. 2014 (2014) 1–18, http://dx.doi.org/10.1155/2014/498762.

[30] S. Ankit, S. B., D. Suman, Image enhancement by histogram technique using matlab, Int. J. Adv. Res. Comp. Comm. Eng. 7 (5) (2018) 346–353.

[31] T. Arici, S. Dikbas, Y. Altunbasak, A histogram modification framework and its application for image contrast enhancement, IEEE Trans. Image Process. 18 (9) (2009) 1921–1935, http://dx.doi.org/10.1109/TIP.2009.2021548.

[32] R. Gonzalez, R. Woods, Digital Image Processing, third ed., Pearson Prentice-Hall, 2009.

[33] Y.-T. Kim, Contrast enhancement using brightness preserving bi-histogram equalization, IEEE Trans. Consum. Electron. 43 (1) (1997) 1–8, http://dx.doi.org/10.1109/30.580378.

[34] K. Zuiderveld, Contrast limited adaptive histogram equalization, Graphics Gems IV (1994) 474–485.

[35] Aqualitas dataset, https://bit.ly/3quTFxg, (Accessed 08 May 2021).

[36] Z. Wang, A. Bovik, H. Sheikh, E. Simoncelli, Image quality assessment: from error visibility to structural similarity, IEEE Trans. Image Process. 13 (4) (2004) 600–612.

[37] S. Paris, S.W. Hasinoff, J. Kautz, Local Laplacian filters: Edge-aware image processing with a Laplacian pyramid, ACM Trans. Graph. 30 (4) (2011) 1–12.

[38] C.S. Xydeas, V. Petrovic, Objective image fusion performance measure, Electron. Lett. 36 (4) (2000) 308–309, http://dx.doi.org/10.1049/el:20000267.

[39] S. B.K., Multifocus and multispectral image fusion based on pixel significance using discrete cosine harmonic wavelet transform, Sig. Image Video Process. 7 (6) (2013) 1125–1143.

[40] S. Li, X. Kang, J. Hu, B. Yang, Image matting for fusion of multi-focus images in dynamic scenes, Inf. Fusion 14 (2) (2013) 147–162.

[41] S. Li, X. Kang, Fast multi-exposure image fusion with median filter and recursive filter, IEEE Trans. Consum. Electron. 58 (2) (2012) 626–632.

[42] V. Vonikakis, O. Bouzos, I. Andreadis, Multi-exposure image fusion based on illumination estimation, in: Proceedings of the IASTED International Conference on Signal and Image Processing and Applications, SIPA, 2011 (January), 2011, pp. 135–142.

[43] M. Chandel, G. Jain, Manganese induced hematological alteration in wistar rats, J. Environ. Occup. Sci. 5 (4) (2016) 77.

[44] Y. Zheng, E.A. Essock, B.C. Hansen, A.M. Haun, A new metric based on extended spatial frequency and its application to DWT based fusion algorithms, Inf. Fusion 8 (2) (2007) 177–192.